International Journal of Plasticity 175 (2024) 103921

Contents lists available at ScienceDirect

International Journal of Plasticity

journal homepage: www.elsevier.com/locate/ijplas

A forming limit framework accounting for various failure mechanisms: Localization, ductile and cleavage fracture

Fuhui Shen [a,b,*], Yannik Sparrer [a], Jing Rao [c], Markus Könemann [a], Sebastian Münstermann [a], Junhe Lian [b,*]

[a] *Institute of Metal Forming, RWTH Aachen University, Intzestraße 10, 52072 Aachen, Germany*
[b] *Advanced Manufacturing and Materials, Department of Mechanical Engineering, Aalto University, Puumiehenkuja 3, 02150 Espoo, Finland*
[c] *Max-Planck-Institut für Eisenforschung, Max-Planck-Straße 1, 40237 Düsseldorf, Germany*

ARTICLE INFO

Keywords:
Forming limits
Stress states
Ductile fracture
Cleavage fracture
Q&P steel

ABSTRACT

The forming limits and failure properties of three distinct advanced high-strength steels (AHSS) have been investigated under various stress states in tensile tests with optimized specimen geometries. In addition to the commonly observed failure patterns governed by localized necking and ductile fracture for two of the AHSS, after substantial plastic deformation at room temperature, cleavage fracture occurs for a large range of stress states in a laboratory quenching and partitioning steel with superior tensile properties. The competition between failure patterns, encompassing ductile and cleavage fractures with and without necking, is governed by the mechanical properties of materials and the stress states, as a transition of failure mechanisms occurs with increasing triaxiality. The forming limit framework is, therefore, further extended to seamlessly integrate cleavage fracture in this study, where the competition between various failure mechanisms is demonstrated using three AHSS in the space of critical strain and principal stress. These findings shed light on the importance of considering cleavage fracture strength as a parameter besides the strength-ductility synergy in advanced high-strength metallic materials, and the proposed framework also gives a more comprehensive guide in designing and conducting the sheet metal forming processes.

1. Introduction

The formation of localized necking has been a critical failure pattern in forming processes of conventional sheet metals. To enhance global formability, i.e., necking resistance, significant efforts have been dedicated to developing advanced metallic materials with high strength, strong strain hardening, and excellent ductility. A particularly successful example is the prosperous development of different generations of advanced high-strength steels (AHSS) offering a vast spectrum of mechanical properties. In pursuing enhanced strength-ductility synergy in metallic materials, ductile fracture has often been encountered in the sheet metal forming of AHSS and other alloys, e.g., the edge crack phenomena (Isik et al., 2014). Consequently, ductile fracture resistance has been recognized as a particularly important factor. The paradigm on the forming limits has been shifted from necking-governed global formability to damage/fracture-controlled local formability (Heibel et al., 2018; Shen et al., 2022b; Tekkaya et al., 2020).

Ductile fracture remains the predominant failure mechanism in typical deformation-based manufacturing processes. The fracture

---

* Corresponding authors.
E-mail addresses: fuhui.shen@ibf.rwth-aachen.de, fuhui.shen@aalto.fi (F. Shen), junhe.lian@aalto.fi (J. Lian).

https://doi.org/10.1016/j.ijplas.2024.103921
Received 2 December 2023; Received in revised form 7 February 2024; Accepted 14 February 2024

initiation strain can be used to quantify the ductile fracture resistance, i.e., local formability, of various high-strength engineering alloys. A common observation is that the ductile fracture strain, determined via fracture tests using optimized specimen geometries, shows pronounced stress state dependence (Brünig et al., 2018; Gao et al., 2023; Habib et al., 2019; Li and Fang, 2022; Li et al., 2011, 2018; Lian et al., 2013; Lou et al., 2014; Roth and Mohr, 2016; Torki et al., 2021; Yang et al., 2022). Various advanced uncoupled ductile fracture models are proposed to provide a more accurate description of the fracture behavior of materials under different stress states by capturing the impacts of stress triaxiality and Lode angle parameter on fracture strain (Bai and Wierzbicki, 2008, 2010; Lou et al., 2017, 2012; Mohr and Marcadet, 2015; Mu et al., 2018; Peng et al., 2021; Quach et al., 2020; Wang and Qu, 2018; Zheng et al., 2023).

Cleavage fracture is another important failure mechanism under monotonic loadings in metals with body center cubic (bcc) and hexagonal close-packed (hcp) structures. Cleavage fracture has not been considered an important failure pattern in metal forming, as it typically only occurs at low or even cryogenic temperatures when the material becomes brittle (Pineau et al., 2016). However, previous studies indicate that an extraordinary amount of plastic deformation occurs in high-strength bcc steels at −196 °C, despite the activation of cleavage fracture (Shen et al., 2022a, 2023). Additionally, a transition of fracture mechanisms from ductile to cleavage can take place at the same temperature by altering the stress state and loading direction (Shen et al., 2022a, 2023; Xiong et al., 2018). These observations indicate significant potential in exploring the formability of materials under more diverse conditions beyond the typical regimes limited by ductile fracture. In this context, the formability of several aluminum alloys is significantly improved under cryogenic forming conditions (Liu and Hao, 2021; Wang et al., 2022; Yuan et al., 2021), which could potentially be applied to steels and other alloys. On the other hand, the development of new metallic materials with high/ultra-high strength raises concerns about the possibility of activating cleavage fracture under normal forming conditions. Therefore, it is also essential to thoroughly analyze the relevance of cleavage fracture in sheet metal forming conditions.

In summary, localized necking and ductile fracture are the two most important failure patterns in the current forming limit framework. Upon the formation of localized necking, the gradual increase of local triaxiality in the necking zone leads to a more critical loading condition for fracture, either ductile or cleavage. Ductile fracture can also occur in some high-strength materials without the formation of localized necking (Chung et al., 2014; Park et al., 2017, 2018; Peng et al., 2017). The competition of localized necking and ductile fracture as failure patterns is affected by both the material properties and stress states (Mu et al., 2020). The current forming limit concept for sheet metals has not incorporated cleavage fracture. However, it is now challenged by forming the new

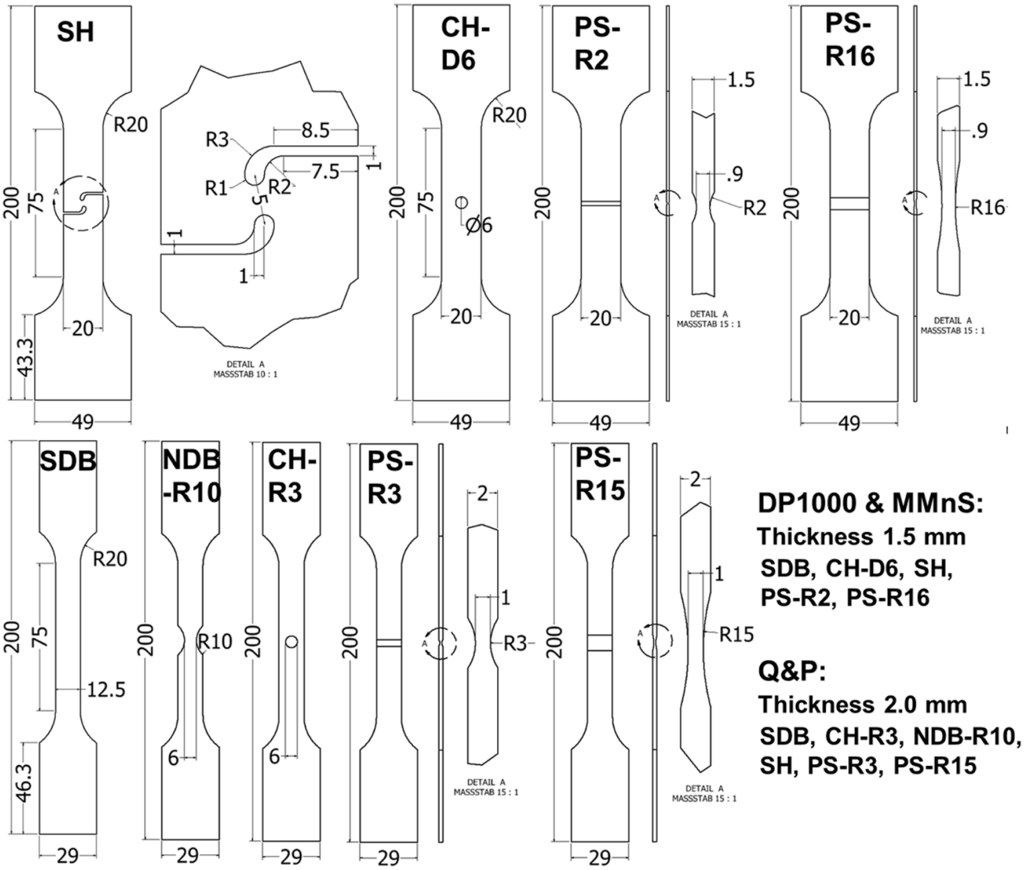

Fig. 1. Geometry of tensile specimens for three different materials (unit: mm).

ultra-high-strength AHSS, for which cleavage is possibly initiated after an enormous amount of plasticity, such as quenching and partitioning (Q&P) steels (Xiong et al., 2018) and medium-Mn steels (MMnS) (Wang et al., 2023) both possessing superior tensile properties. Therefore, in this study, we aim to extend the current forming limit theory to a general framework by incorporating cleavage fracture. The competition between instability, ductile fracture, and cleavage fracture is demonstrated using various AHSS and modeled by the newly proposed framework.

In the following, the mechanical testing program and experimental results of three different AHSS are described in Chapter 2 and 3. The theoretical formulation of the forming limit framework is elaborated in Chapter 4. The methodology to calibrate and validate material parameters is provided in Chapter 5, followed by the fracture prediction for different AHSS in Chapter 6. A detailed elaboration of the forming limit framework considering the competition of different failure mechanisms is provided in Chapter 7.

2. Materials and mechanical tests

The forming and failure properties of three different types of advanced high-strength steels have been investigated in this study. The reference material chosen is a commercial DP1000, representing the 1st generation of AHSS, featuring a dual-phase ferrite and martensite microstructure (Liu et al., 2020a). The focus of this study centers on the fracture behavior of two promising candidates from the 3rd generation of AHSS, an intercritically annealed MMnS and a Q&P steel. Both MMnS and Q&P steel are produced in the laboratory. The microstructure of the MMnS (4.00 wt.% Mn) is composed of austenite and ferrite (Shen et al., 2022b). The microstructure of the Q&P (4.34 wt.% Mn) steel is composed of austenite and martensite.

To assess the plasticity and fracture properties of these AHSS under typical stress states relevant to metal forming, fracture tests were conducted at room temperature utilizing various flat tensile specimens produced by electrical discharge machining (EDM), as depicted in Fig. 1, following EN ISO 6892–1:2016. For each material, plane strain (PS), shear (SH), and central hole (CH) geometries were employed. One notched dog bone (NDB) geometry was additionally used to quantitatively determine the fracture properties of the Q&P steel. Quasistatic loading conditions were maintained and the crosshead velocity was 0.2 mm/min. Despite the variation of applied notch radi for each material, the Q&P specimens differed in thickness and width compared to the other two materials. The flat specimens' thickness is 1.5 mm for DP1000 and MMnS, and 2 mm for Q&P steel. The flat specimens' width of the central part is 20 mm for DP1000 and MMnS, and 12.5 mm for Q&P steel. The gage length during tensile tests was 30 mm for the CH-D6 specimens of the DP1000 and MMnS, which was 40 mm for all other tensile specimens. Two repeating tests were performed for each testing condition. Further elaboration regarding the experimental configuration can be found in previous studies (Liu et al., 2020b; Shen et al., 2022b) for the DP1000 and MMnS.

To evaluate the effects of anisotropy, uniaxial tensile tests were performed for the DP1000 using the smooth dog bone (SDB) specimens manufactured along the rolling (RD), diagonal (DD) and transverse (TD) directions. Minor anisotropic effects exist in DP1000 according to the tensile properties provided in Fig. A1 and Table A1. Due to the limitation in the width of the rolling strips produced in the lab, the tensile properties along other directions were not investigated for MMnS and Q&P steel. Therefore, all three materials were assumed to be isotropic for simplicity in this study. The results presented in the study are based on mechanical tests along the rolling direction unless otherwise stated.

3. Tensile properties and fracture mechanisms

The comparison of uniaxial tensile properties of three AHSS is presented in Fig. 2 and Table 1. Both laboratory MMnS and Q&P steel, representing the 3G-AHSS, demonstrate superior tensile properties compared to DP1000. The presence of austenite in the microstructure contributes to enhanced strain hardening properties of MMnS and Q&P steels, resulting in improved necking resistance and higher uniform elongation in comparison to DP1000. The jerky flow exhibited by the MMnS is attributed to the dynamic strain aging mechanism, commonly observed under a specific combination of temperature and strain rates in intercritically annealed MMnS

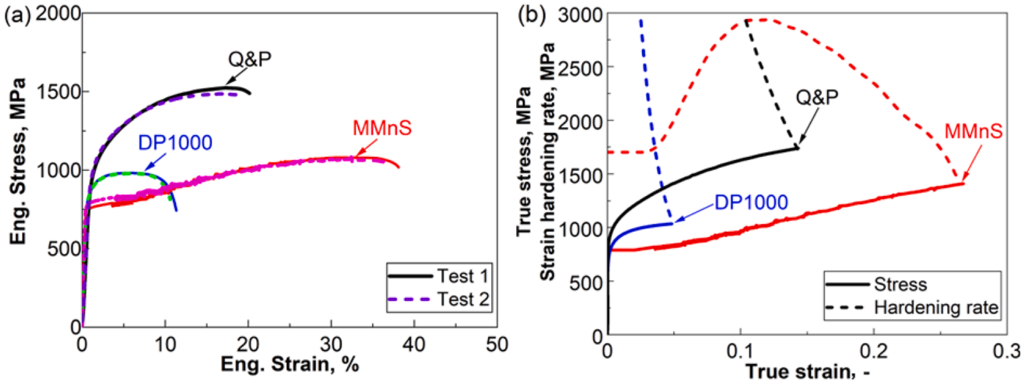

Fig. 2. Uniaxial tensile properties of the investigated AHSS: (a) engineering stress-strain curves, and (b) true stress-strain curves and strain hardening behavior based on test 1.

Table 1
Comparison of uniaxial tensile characteristics of investigated AHSS.

Material		Yield strength (YS), MPa	Ultimate tensile strength (UTS), MPa	Uniform elongation (UE),%	Total elongation (TE),%	Work at uniform elongation, MPa × %	Work at total elongation, MPa × %
DP1000	Test 1	780.9	981.0	4.9	11.0	4882.5	10,429.6
	Test 2	777.8	978.4	5.3	10.2	5065.1	10,461.7
MMnS	Test 1	789.3	1080.6	32.8	38.0	30,855.1	36,462.6
	Test 2	820.4	1083.0	32.4	36.3	30,580.4	34,695.0
Q&P	Test 1	918.2	1523.1	17.4	20.2	23,018.6	27,272.8
	Test 2	942.6	1485.7	17.1	18.6	22,412.0	24,682.4

(Yang et al., 2018) and other alloys (Jacobs et al., 2019; Li et al., 2022; Shen et al., 2020). The MMnS exhibits the largest uniform elongation (UE) and total elongation (TE) among all three AHSS materials. The Q&P steel showcases higher yield strength (YS) and ultimate tensile strength (UTS), leading to an excellent strength-ductility synergy compared to the other two materials. The integration of the engineering stress-strain curves until uniform elongation and total elongation is employed as quantitative parameters to evaluate the energy consumption capacity, which is relevant for toughness assessment. The MMnS and Q&P steel can consume significantly more energy at UE and TE than DP1000, as listed in Table 1. However, it is worth noting that a sufficient load-carrying capacity is maintained in DP1000 for a relatively larger post-necking strain range than the other two AHSS before reaching the complete rupture of the specimens.

Previous studies have shown minimal scatter in the fracture properties of DP1000 and MMnS in repeating tests (Liu et al., 2020b; Shen et al., 2022b). The DP1000 and MMnS exhibit typical void-mediated ductile failure mechanisms. In contrast, for the investigated Q&P steel, relatively good repeatability is observed solely in the elastoplastic deformation properties, as there is a significant scatter (represented by color band) in the fracture displacements of the same sample geometry, as presented in Fig. 3. For the shear specimens of DP1000 and MMnS, the fracture was initiated in the central ligament of the SH specimens subjected to the shear loading condition. Some studies show that the crack can initiate from the free boundaries of this type of shear geometry (Peirs et al., 2011; Rahmaan et al., 2017; Roth and Mohr, 2018). The initiation of ductile fracture from either the center (shear loading) or the free edge (tension loading) of the SH geometry is controlled by the stress state dependence of ductile fracture strain and the strain hardening properties of the material (Roth and Mohr, 2018). However, the crack initiation at the notch root in the SH specimens of the investigated Q&P steel in this study is attributed to the different failure mechanisms, as shown in Fig. 4. The postmortem analysis revealed that the investigated Q&P steel experienced cleavage fracture at room temperature after significant plastic deformation. In particular, as depicted in Fig. 4, the intergranular fracture is the dominant failure mode across various stress states, which indicates that the fracture resistance of grain boundaries is weaker than the matrix of the investigated laboratory Q&P steel. These experimental observations highlight the potential emergence of cleavage fracture as another critical failure pattern in sheet metal forming of materials with promising tensile properties, particularly relevant to next-generation AHSS.

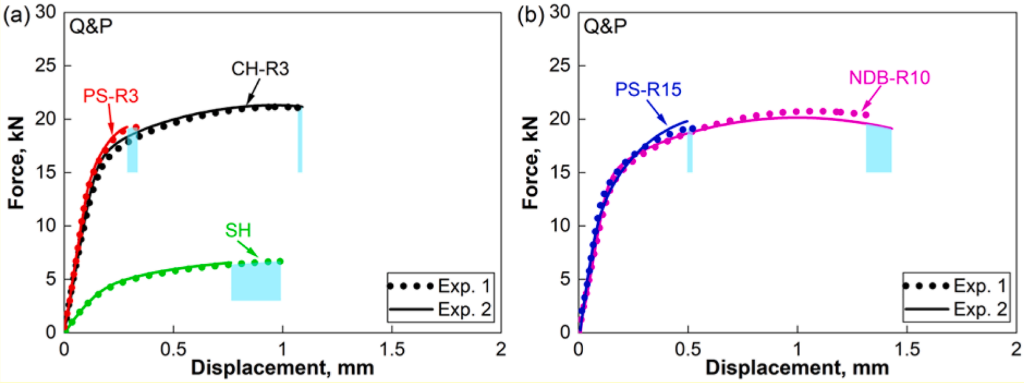

Fig. 3. Experimental force and displacement curves of the investigated Q&P steel in tensile tests using different specimens: (a) SH, PS-R3 and CH-R3; (b) PS-R15 and NDB-R10. The color band represents the scatter of fracture displacements.

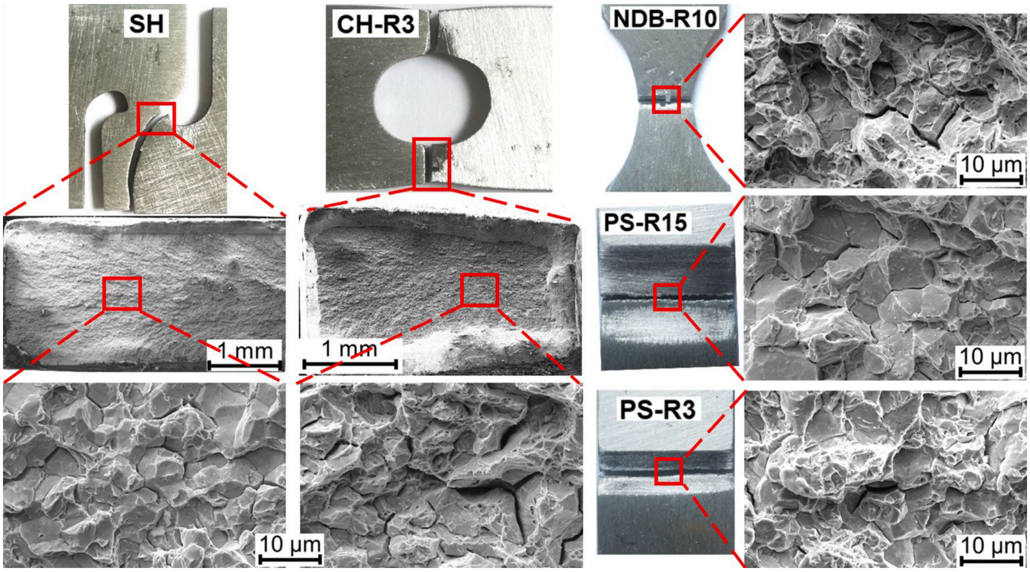

Fig. 4. Fracture mechanisms of the investigated Q&P steel in different tensile specimens.

4. A forming limit framework accounting for various failure mechanisms

4.1. A unified fracture criterion

The forming limit curve at ductile fracture $\mathrm{FLC_{df}}$ is a commonly utilized tool for characterizing the local formability of sheet metals, where ductile fracture plays a more critical role than necking. In recently developed uncoupled ductile fracture models, the influence of stress state on ductile fracture strain $\overline{\varepsilon}_{\mathrm{df}}$ is quantitatively captured using various phenomenological or mechanism-motivated formulations (Bai and Wierzbicki, 2008, 2010; Khan and Liu, 2012; Li and Fang, 2022; Lou et al., 2012; Mohr and Marcadet, 2015; Mu et al., 2018; Peng et al., 2021; Zheng et al., 2023). The stress triaxiality η and Lode angle parameter $\overline{\theta}$, derived from stress invariants I_1, J_2, J_3, are the most frequently used variables in this context. The ductile fracture indicator I_{df} is used in a general form considering non-proportional loading effects. Any ductile fracture models can be flexibly integrated into the unified fracture criterion. The phenomenological function, initially proposed by Bai and Wierzbicki (2008) via adding the Lode angle effects to the widely applied Johnson-Cook criterion (Johnson and Cook, 1985), is adopted in this study to quantify the stress state dependence of ductile fracture strain. There are four parameters $F_{1\sim4}$ to be calibrated based on fracture tests, assuming the fracture locus is symmetric with respect to Lode angle parameter. There are studies showing the existence of cutoff triaxiality η_{c}, below which ductile fracture does not occur (Bao and Wierzbicki, 2005; Lou et al., 2014). Based on the fracture phenomena under negative triaxiality conditions, the cutoff triaxiality has been observed to have linear (Brünig et al., 2018) or nonlinear (Lou et al., 2014) dependence on the Lode parameter. Due to the lack of experimental results under highly negative triaxiality conditions for the investigated AHSS, a constant cutoff value $\eta_{\mathrm{c}} = -\frac{1}{3}$ is considered in this study (Bao and Wierzbicki, 2005).

$$\eta = \frac{I_1}{3\sqrt{3J_2}} \quad \overline{\theta} = 1 - \frac{2}{\pi}\cos^{-1}\left(\frac{3\sqrt{3}}{2}\frac{J_3}{J_2^{3/2}}\right) \tag{1}$$

$$I_{\mathrm{df}} = \int_0^{\overline{\varepsilon}^{\mathrm{p}}} \frac{d\overline{\varepsilon}^{\mathrm{p}}}{\overline{\varepsilon}_{\mathrm{df}}(\eta,\ \overline{\theta})} \tag{2}$$

$$\overline{\varepsilon}_{\mathrm{df}} = w(\eta,\ \overline{\theta}) = \begin{cases} +\infty & \eta \le \eta_{\mathrm{c}} \\ \left(F_1 exp^{-F_2\eta} - F_3 exp^{-F_4\eta}\right)\overline{\theta}^2 + F_3 exp^{-F_4\eta} & \eta > \eta_{\mathrm{c}} \end{cases} \tag{3}$$

Cleavage fracture can be another relevant failure pattern that limits the formability of certain metallic materials, particularly high/ultra-high strength steels with bcc structures. Microscopic defects (cracks) exist in typical engineering metallic materials, leading to crack propagation as the critical step of the cleavage fracture process. For cracks to propagate in the cleavage mode across the most critical microstructural barrier, the threshold value of the maximum principal stress σ_1 must be surpassed, which is referred to as a material property, the cleavage fracture strength σ_{c} (Beremin, 1983; Orowan, 1949; Pineau et al., 2016). Due to the heterogeneity of microstructure and defects in the material, the failure probability concept, such as the Weibull distribution function, is widely utilized to account for the stochastic nature of σ_{c}.

$$P_\mathrm{f} = 1 - exp\left[-\left(\frac{\sigma_\mathrm{c} - \sigma_\mathrm{min}}{\sigma_\mathrm{u} - \sigma_\mathrm{min}}\right)^m\right] \text{ (Weibull distribution)} \tag{4}$$

Shen et al. (2022a) have observed a stress-state-dependent competition between cleavage and ductile fracture mechanisms and proposed a unified fracture criterion, which has been extended to encompass the impacts of anisotropy on the competition of fracture mechanisms (Shen et al., 2023). When employing the Mises plasticity model, the principal stress ($\sigma_1 > \sigma_2 > \sigma_3$) can be formulated as functions of η and $\overline{\theta}$, as shown in Eq. (5)-(7) (Bai and Wierzbicki, 2010). Consequently, the cleavage failure criterion ($\sigma_1 \geq \sigma_\mathrm{c}$) can be reformulated as a critical equivalent plastic strain $\overline{\varepsilon}_{\sigma_1=\sigma_\mathrm{c}}$ through substituting the Mises equivalent stress $\overline{\sigma}_\mathrm{v}$ with the flow stress. The analytical equations of the critical cleavage fracture strain are expressed in Eq. (8) and (9) for Swift and Voce hardening laws, respectively, which indicate that the critical cleavage fracture strain is dependent on stress states and strain hardening behavior. It is noted that the cutoff value $\eta_\mathrm{c} = -\frac{1}{3}$ is intrinsically embedded in the cleavage fracture criterion, as cleavage fracture only occurs under tensile modes.

$$\sigma_1 = \left\{\eta + \frac{2}{3} cos\left[\frac{\pi}{6}(1-\overline{\theta})\right]\right\}\overline{\sigma}_\mathrm{v} \tag{5}$$

$$\sigma_2 = \left\{\eta + \frac{2}{3} cos\left[\frac{\pi}{6}(3+\overline{\theta})\right]\right\}\overline{\sigma}_\mathrm{v} \tag{6}$$

$$\sigma_3 = \left\{\eta - \frac{2}{3} cos\left[\frac{\pi}{6}(1+\overline{\theta})\right]\right\}\overline{\sigma}_\mathrm{v} \tag{7}$$

$$\begin{aligned} \overline{\sigma}_\mathrm{v} &= A\cdot(\overline{\varepsilon}^\mathrm{p} + \overline{\varepsilon}_0^\mathrm{p})^n \text{ (Swift)} \\ \overline{\varepsilon}_{\sigma_1=\sigma_\mathrm{c}} &= \left(\frac{\sigma_\mathrm{c}}{A\left\{\eta + \frac{2}{3}\cos\left[\frac{\pi}{6}(1-\overline{\theta})\right]\right\}}\right)^{1/n} - \overline{\varepsilon}_0^\mathrm{p} \end{aligned} \tag{8}$$

$$\begin{aligned} \overline{\sigma}_\mathrm{v} &= k_0 + Q\cdot(1 - \exp(-\gamma\cdot\overline{\varepsilon}^\mathrm{p})) \text{ (Voce)} \\ \overline{\varepsilon}_{\sigma_1=\sigma_\mathrm{c}} &= -\left\{ln\left[1 - \left(\frac{\sigma_\mathrm{c}}{\eta + \frac{2}{3}\cos\left[\frac{\pi}{6}(1-\overline{\theta})\right]} - k_0\right)\Big/ Q\right]\right\}\Big/\gamma \end{aligned} \tag{9}$$

Under a specific loading condition, i.e., stress state, temperature, and strain rate, the competition between ductile and cleavage fracture is governed by which failure criterion is satisfied first. Cleavage is prone to occur under high triaxial loading conditions, as the maximum principal stress increases with triaxiality at the same equivalent plastic strain value, as indicated by Eq. (5). From an energy dissipation perspective, cleavage fracture becomes the preferred failure mode due to its significantly faster energy release rate. The existing microcracks in the material and those initiated during deformation will propagate in the cleavage mode if the propagation criterion is fulfilled ($\sigma_1 \geq \sigma_\mathrm{c}$). Otherwise, microcracks blunt to form voids, and ductile fracture takes place after reaching the ductile failure criterion ($I_\mathrm{df} \geq 1$) via the void growth and coalescence. The nucleation and blunting of cracks and the related change of stress fields on the microscopic scale are not considered in the finite element simulations based on continuum mechanics approaches in this study. Therefore, under proportional loadings, the competition between cleavage and ductile fracture is essentially controlled by comparing $\overline{\varepsilon}_{\sigma_1=\sigma_\mathrm{c}}$ and $\overline{\varepsilon}_\mathrm{df}$ for the specific stress state. For a more general loading scenario, the unified fracture criterion, which considers the competition between these two failure mechanisms, can be expressed using a damage status variable D. This variable takes the value of zero for the virginal state and one for the fractured condition.

$$D = \begin{cases} 0 & \eta \leq \eta_\mathrm{c} & \text{i) No fracture} \\ \left.\begin{array}{ll} 0 & I_\mathrm{df} < 1 \ \wedge \ \eta_\mathrm{c} < \eta \ \wedge \ \overline{\varepsilon} < \overline{\varepsilon}_{\sigma_1=\sigma_\mathrm{c}} \ (\sigma_1 < \sigma_\mathrm{c}) \\ 1 & I_\mathrm{df} \geq 1 \ \wedge \ \eta_\mathrm{c} < \eta \ \wedge \ \overline{\varepsilon} < \overline{\varepsilon}_{\sigma_1=\sigma_\mathrm{c}} \ (\sigma_1 < \sigma_\mathrm{c}) \end{array}\right\} & & \text{ii) Ductile fracture} \\ 1 & \eta_\mathrm{c} < \eta \ \wedge \ \overline{\varepsilon} \geq \overline{\varepsilon}_{\sigma_1=\sigma_\mathrm{c}} \ (\sigma_1 \geq \sigma_\mathrm{c}) & \text{iii) Cleavage fracture} \end{cases} \tag{10}$$

4.2. *Forming limits by localization*

Localized deformation is a typical failure pattern that limits the global formability of conventional ductile sheet metals. For the theoretical calculation of forming limit curves at necking (FLC$_\mathrm{n}$), the classical modified maximum force criterion (MMFC) proposed by Hora et al. (2011) is employed in this study directly based on the flow curve without calibrating additional parameters, such as the imperfection ratio in the Marciniak and Kuczyński (1967) (MK) model. The strain increment ratio ($\beta = \frac{\Delta\varepsilon_2}{\Delta\varepsilon_1}$) and the stress ratio ($\alpha = \frac{\sigma_2}{\sigma_1}$)

are two important variables to define the strain path in the MMFC. When the Mises model is employed, the relationship between these two parameters is:

$$\alpha(\beta) = \frac{2 \cdot \beta + 1}{\beta + 2} \; \beta(\alpha) = \frac{2 \cdot \alpha - 1}{2 - \alpha} \; \frac{\partial \beta}{\partial \alpha} = \frac{3}{(2 - \alpha)^2} \tag{11}$$

According to the Considère criterion, the instability (diffusive necking) in uniaxial tension of ductile metals occurs at the intersection of the flow curve (σ_1 plotted over ε_1) with the strain hardening curve ($\frac{\partial \sigma_1}{\partial \varepsilon_1}$ plotted over ε_1). It has been observed in experiments that the local stress state gradually evolves towards the plane strain tension condition (localized necking defined as $\beta = 0$) as deformation progresses beyond the uniform stage. The additional contribution due to change in strain path ($\frac{\partial \sigma_1}{\partial \beta} \frac{\partial \beta}{\partial \varepsilon_1}$) is considered in the MMFC, which is formulated as follows:

$$\frac{\partial \sigma_1}{\partial \varepsilon_1} + \frac{\partial \sigma_1}{\partial \beta} \frac{\partial \beta}{\partial \varepsilon_1} = \sigma_1 \tag{12}$$

$$\Delta \beta = \frac{\sigma_1 - f(\alpha) \cdot f(\alpha) \cdot (1 + \alpha \cdot \beta) \cdot H'}{f'(\alpha) \cdot H \Big/ \left(\frac{\partial \beta}{\partial \alpha} \right)} \cdot \Delta \varepsilon_1 \tag{13}$$

H and H' are the flow stress and strain hardening rate of the material. When the Mises plasticity model is applied, the stress ratio-related variable $f(\alpha) = \frac{\sigma_1}{\sigma_v}$ and its derivative $f'(\alpha) = \frac{\partial f(\alpha)}{\partial \alpha}$ can be expressed as:

$$f(\alpha) = \left(1 + \alpha^2 - \alpha\right)^{-\frac{1}{2}} f'(\alpha) = (0.5 - \alpha)\left(1 + \alpha^2 - \alpha\right)^{-\frac{3}{2}} \tag{14}$$

Under the plane stress conditions relevant to the FLC$_\mathrm{n}$ ($\sigma_3 = 0$), the stress triaxiality and Lode angle parameter are related to each other by setting the principal stress as zero according to Eq. (7). Both η and $\overline{\theta}$ can be expressed by the stress ratio α. Consequently, the FLC$_\mathrm{n}$ is presented as critical equivalent plastic strain over η and $\overline{\theta}$, which can be independently evaluated regardless of the fracture mechanisms in the forming limit framework.

$$\eta = \left(\frac{1 + \alpha}{3}\right)\left(1 + \alpha^2 - \alpha\right)^{-\frac{1}{2}} \overline{\theta} = \frac{6}{\pi}\left[\arccos\left(\frac{3\eta}{2}\right)\right] - 1 \tag{15}$$

5. Determination of critical stress and strain variables

The isotropic Mises plasticity model has been employed to determine critical stress and strain variables of investigated AHSS in finite element simulations. The critical regions of tensile specimens have been discretized using fine eight-node brick elements with reduced integration points (C3D8R, element size 0.1 × 0.1 × 0.1 mm^3) in the ABAQUS/Explicit software. Coarser elements have been used in other regions of the finite element models with symmetry in the thickness direction to reduce the computational cost. Utilizing the combined Swift-Voce hardening law, the strain hardening parameters of investigated AHSS have been calibrated, as summarized in Table 2, where A, $\overline{\varepsilon}_0^\mathrm{p}$, n are parameters of the Swift function and k_0, Q, γ are parameters of the Voce function and λ is the weight parameter. Based on the flow curve depicted in Fig. 5, the local stress and strain variables at fracture moments can be obtained from the finite element simulations with high accuracy, as shown in Fig. 6 for the Q&P steel. The instantaneous values of equivalent plastic strain (PEEQ), η and $\overline{\theta}$ in the critical elements (CE) of tensile specimens corresponding to fracture displacements are compiled in Table 3. The average stress triaxiality η_avg and Lode angle parameter $\overline{\theta}_\mathrm{avg}$, calculated by integration over the deformation history, serve as descriptors to elucidate the holistic stress state of the specimens (Shen et al., 2022b; Wu et al., 2017). As cleavage fracture is initiated in the investigated Q&P steel, it is essential to ascertain the cleavage fracture strength σ_c. The critical values of σ_1 taken from two positions, the critical elements and the elements with the peak σ_1, are also summarized in Table 3 for all geometries. As depicted in Fig. 6, σ_1 exhibits its highest value at the notch root of the shear specimen of the Q&P steel. For the CH-R3 geometry of the Q&P steel, the σ_1 reaches its peak slightly off the notch root, corresponding to the highest local triaxiality point. The position of the peak σ_1 aligns with the CE in other geometries.

Table 2
Calibrated strain hardening parameters for investigated AHSS.

Material	$\sigma = \lambda \cdot \sigma_\mathrm{Swift} + (1 - \lambda) \cdot \sigma_\mathrm{Voce}$						
	$\sigma_\mathrm{Swift} = A \cdot (\overline{\varepsilon}^\mathrm{p} + \overline{\varepsilon}_0^\mathrm{p})^n$			$\sigma_\mathrm{Voce} = k_0 + Q \cdot (1 - exp(-\gamma \cdot \overline{\varepsilon}^\mathrm{p}))$			
	A	$\overline{\varepsilon}_0^\mathrm{p}$	n	λ	k_0	Q	γ
DP1000	1300	0.000	0.075	0.5	773.28	266.19	73.94
MMnS	2720	0.207	0.866	1.0	640.60	2400.00	1.56
Q&P	2572	0.004	0.204	0.0	982.70	876.70	13.54

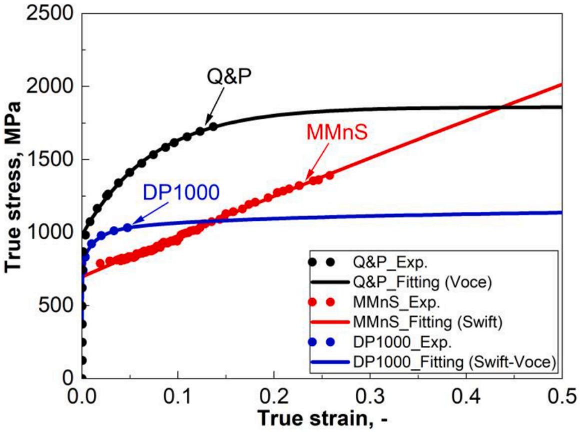

Fig. 5. Calibrated strain hardening curves of investigated AHSS.

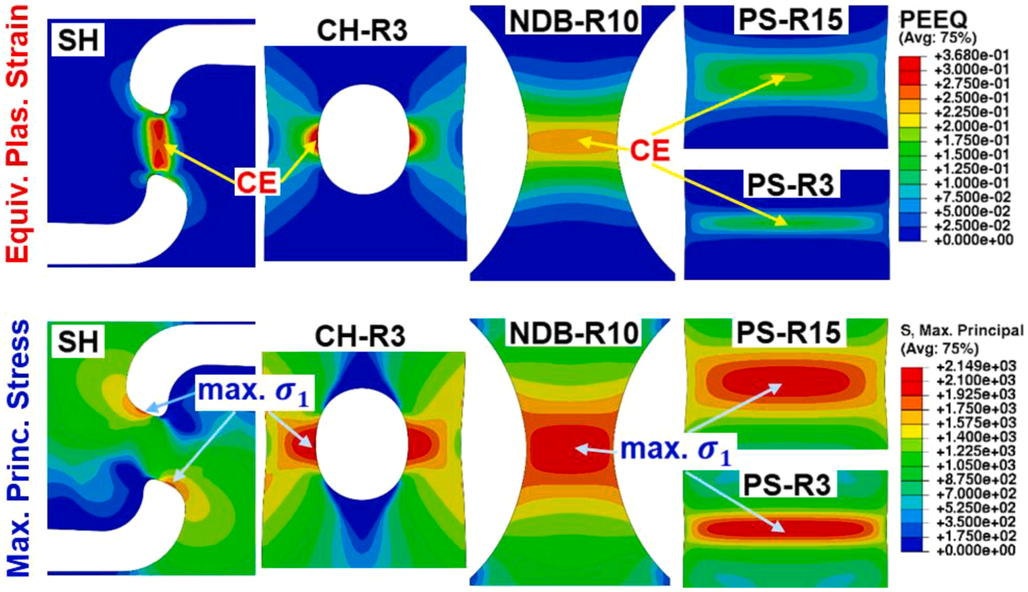

Fig. 6. Predicted contours of equivalent plastic strain and maximum principal stress on the mid-thickness plane of tensile specimens of Q&P steel at fracture displacements.

6. Fracture prediction of different AHSS

Since fracture initiation is accompanied by substantial plastic deformation in the Q&P steel, the critical strain-based fracture criterion has also been selected as the straightforward approach to predict the fracture properties of the Q&P steel in tensile tests. The parameters ($F_1 \sim F_4$) in the strain-based fracture initiation locus of the investigated Q&P steel, in Fig. 7(a), have been optimized based on local strain values taken from critical elements, as listed in Table 4. The strain-based ductile fracture initiation locus parameters of DP1000 and MMnS determined in previous studies are also provided in Table 4 (Liu et al., 2020b; Shen et al., 2022b). The global fracture displacements in different specimens of the investigated three AHSS, depicted in Fig. 8, can be well captured using the strain-based criterion.

Alternatively, the critical stress-based fracture criterion ($\sigma_1 \geq \sigma_c$) has been used to simulate the fracture behavior of the Q&P steel, considering the cleavage fracture mechanism. The values of σ_1 at fracture taken from elements with the peak σ_1 in all five geometries with two repeating tests, as summarized in Table 3, have been sorted in ascending order. The corresponding failure probability for the $\#i$ test is determined as $P_f^i = \frac{i-0.3}{N+0.4}$, where N is the number of all tests (ten in this study). The probabilistic distribution of cleavage fracture strength of the investigated Q&P steel is represented by the Weibull distribution function $P_f = 1 - \exp\left[-\left(\frac{\sigma_1-1890}{2202-1890}\right)^2\right]$, as shown in Fig. 7(b). The cleavage fracture strength of the investigated Q&P steel is determined to be 2150 MPa ($P_f = 50\%$). As shown in Fig. 8(d), the global fracture displacements of the Q&P steel can be well captured when only the cleavage fracture strength criterion is

Table 3
The local stress state variables at the fracture moment.

Material	Specimen	η_{avg}	$\bar{\theta}_{avg}$	η	$\bar{\theta}$	PEEQ	σ_1 (MPa)
DP1000	CH-D6 (CE)	0.49	0.93	0.51	0.91	1.03	1368.03
	CH-D6 (max. σ_1)	0.56	0.65	0.83	0.59	0.85	1720.82
	SH (CE)	0.02	−0.01	0.26	0.13	1.97	1022.46
	SH (max. σ_1)	−0.40	−0.14	0.87	0.45	1.19	1773.58
	PS-R16 (CE)	0.75	0.02	0.88	0.00	0.76	1668.86
	PS-R2 (CE)	0.89	0.02	0.98	0.00	0.63	1778.68
MMnS	CH-D6 (CE)	0.34	0.98	0.34	0.99	0.48	1991.74
	SH (CE)	0.00	−0.01	0.06	0.14	0.40	1152.69
	SH (max. σ_1)	0.38	0.89	0.35	0.99	0.47	1966.80
	PS-R16 (CE)	0.56	0.14	0.52	0.33	0.25	1589.40
	PS-R2 (CE)	0.69	0.08	0.62	0.30	0.21	1577.66
Q&P (Test 1)	CH-R3 (CE)	0.35	0.97	0.35	0.97	0.46	1874.84
	CH-R3 (max. σ_1)	0.50	0.81	0.58	0.85	0.30	2297.35
	SH (CE)	0.00	−0.04	0.04	0.00	0.28	1129.24
	SH (max. σ_1)	0.55	0.52	0.55	0.53	0.15	2082.78
	NDB-R10 (max. σ_1)	0.45	0.68	0.52	0.56	0.24	2128.22
	PS-R15 (max. σ_1)	0.54	0.30	0.57	0.20	0.15	2064.98
	PS-R3 (max. σ_1)	0.67	0.06	0.69	0.02	0.17	2249.75
Q&P (Test 2)	CH-R3 (CE)	0.33	0.97	0.34	0.97	0.47	1875.89
	CH-R3 (max. σ_1)	0.49	0.81	0.59	0.85	0.31	2312.00
	SH (CE)	−0.01	−0.03	0.01	−0.02	0.18	1030.07
	SH (max. σ_1)	0.53	0.53	0.53	0.54	0.11	1975.29
	NDB-R10 (max. σ_1)	0.48	0.64	0.56	0.51	0.29	2217.46
	PS-R15 (max. σ_1)	0.54	0.31	0.56	0.23	0.14	2030.56
	PS-R3 (max. σ_1)	0.65	0.09	0.68	0.03	0.12	2135.64

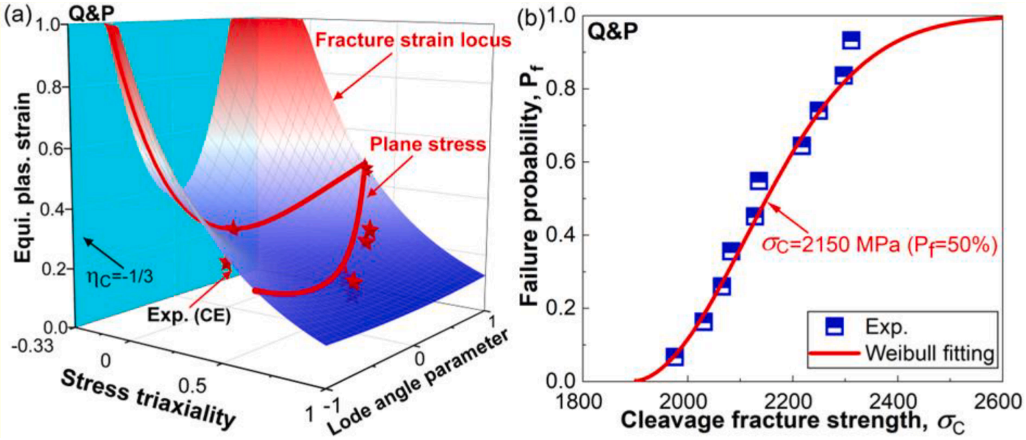

Fig. 7. Calibrated fracture criterion of investigated Q&P steel: (a) strain-based fracture initiation locus and (b) Weibull distribution of cleavage fracture strength.

Table 4
Calibrated parameters in the unified fracture criterion of investigated AHSS.

Material	F_1	F_2	F_3	F_4	σ_u	σ_{min}	m
DP1000	2.12	1.41	2.06	1.32	–	–	–
MMnS	0.54	0.35	0.40	0.98	–	–	–
Q&P	0.93	1.99	0.28	0.91	2202	1890	2

applied. By adopting the failure probability concept, the predicted range of fracture displacements (color bands) aligns well with the experimental results.

The typical shear fracture path in the ligament of the SH specimen is predicted when the critical strain-based fracture initiation criterion is applied, in agreement with the experimental crack paths of DP1000 and MMnS. However, the crack was initiated at the notch root in the SH specimens of the Q&P steel during experiments, which cannot be reproduced using the critical strain-based failure criterion with four parameters given in Table 4, as shown in Fig. 9. Based on the contour of the ductile fracture indicator I_{df} right before

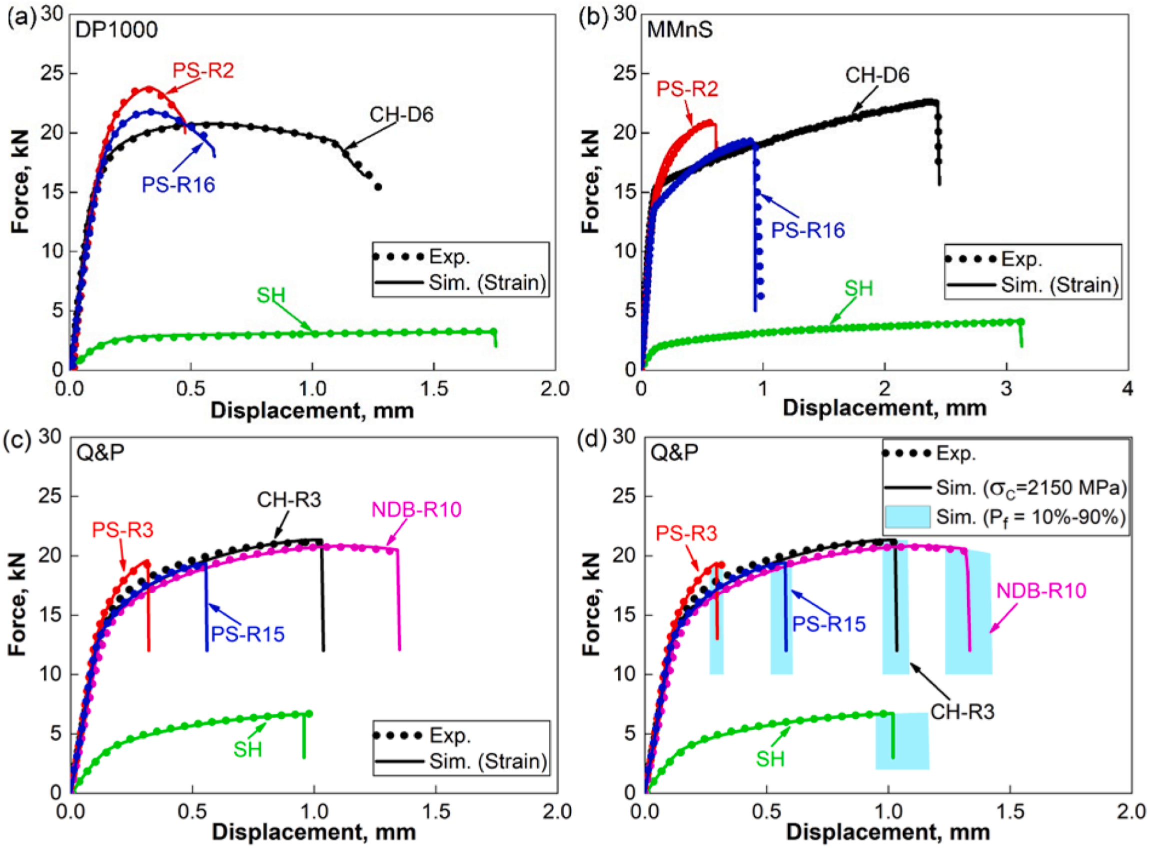

Fig. 8. Force and displacement results of tensile tests predicted using the critical strain-based criterion for (a) DP1000, (b) MMnS and (c) Q&P steel, and using only the cleavage fracture strength criterion ($\sigma_1 \geq \sigma_c$) for (d) Q&P steel.

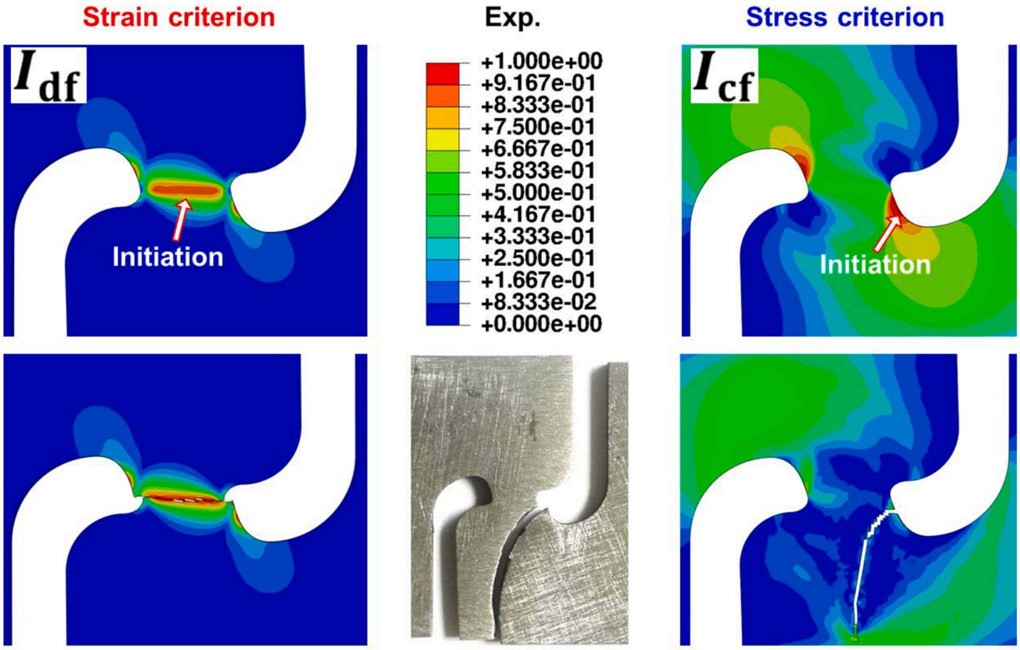

Fig. 9. Comparison of the crack initiation location and propagation paths in shear specimens of the Q&P steel between experimental and numerical results using critical strain-based criterion and only cleavage fracture strength criterion. (contours plotted on med-thickness plane).

crack initiation, as shown in Fig. 9, it is concluded that crack initiation occurs at the center of the SH geometry of the Q&P steel when the critical strain-based criterion is applied in the simulations. In this case, the crack propagates in the shear region. Since only the critical value of the maximum principal stress is applied in the failure mechanism-informed cleavage fracture strength criterion, the probability of triggering cleavage fracture can be evaluated using the cleavage fracture indicator, which is defined as the normalized ratio $I_{\text{cf}} = \frac{\sigma_1}{\sigma_c}$. Cleavage fracture occurs when I_{cf} reaches one. For the visualization purpose, I_{cf} takes the value of zero when $\sigma_1 \leq 0$. Based on the contour of cleavage fracture indicator I_{cf} right before crack initiation, as shown in Fig. 9, it is concluded that crack initiation occurs at the notch root in the SH specimens of the Q&P steel, corresponding to the peak value of the σ_1, when only the stress based cleavage fracture criterion is applied in the simulations. The crack then propagates along the path that maximizes the energy release rate, namely approximately following the mode I pattern, which aligns with experimental results. A slightly higher value of

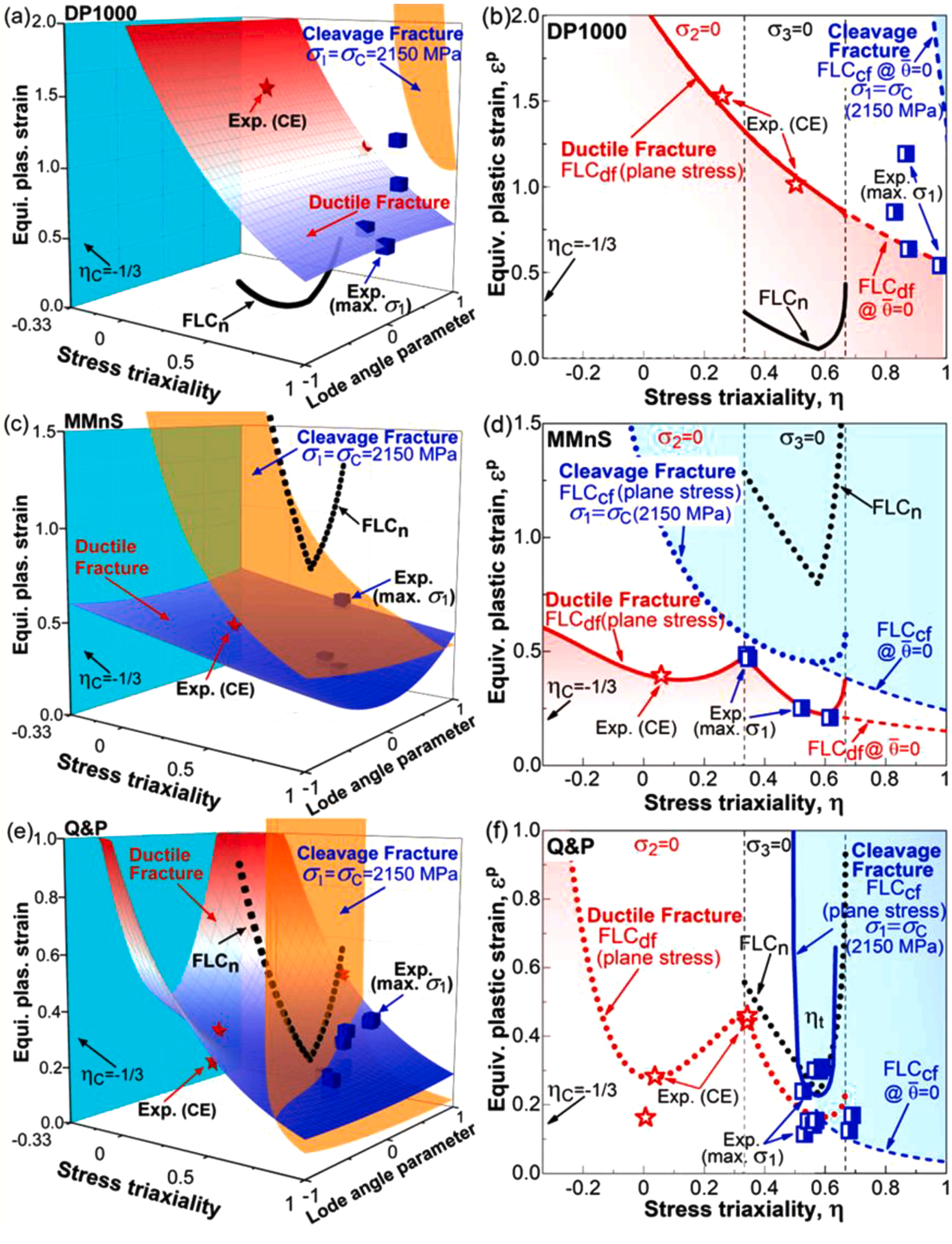

Fig. 10. The forming limit framework considering different failure patterns demonstrated as stress state dependent critical equivalent plastic strain for three AHSS. (a) and (b) DP1000, (c) and (d) MMnS, (e) and (f) Q&P steel.

cleavage fracture strength is assigned to the upper part of the finite element model to reproduce the exact crack initiation position as in experiments.

Although the global fracture displacements can be well captured using advanced strain-based fracture criteria, significant errors could occur in the prediction of local fracture patterns when the underlying failure mechanisms are overlooked. It is thus essential to develop a unified forming limit framework that also considers the cleavage mechanism to simulate the fracture properties of AHSS under sheet metal forming conditions.

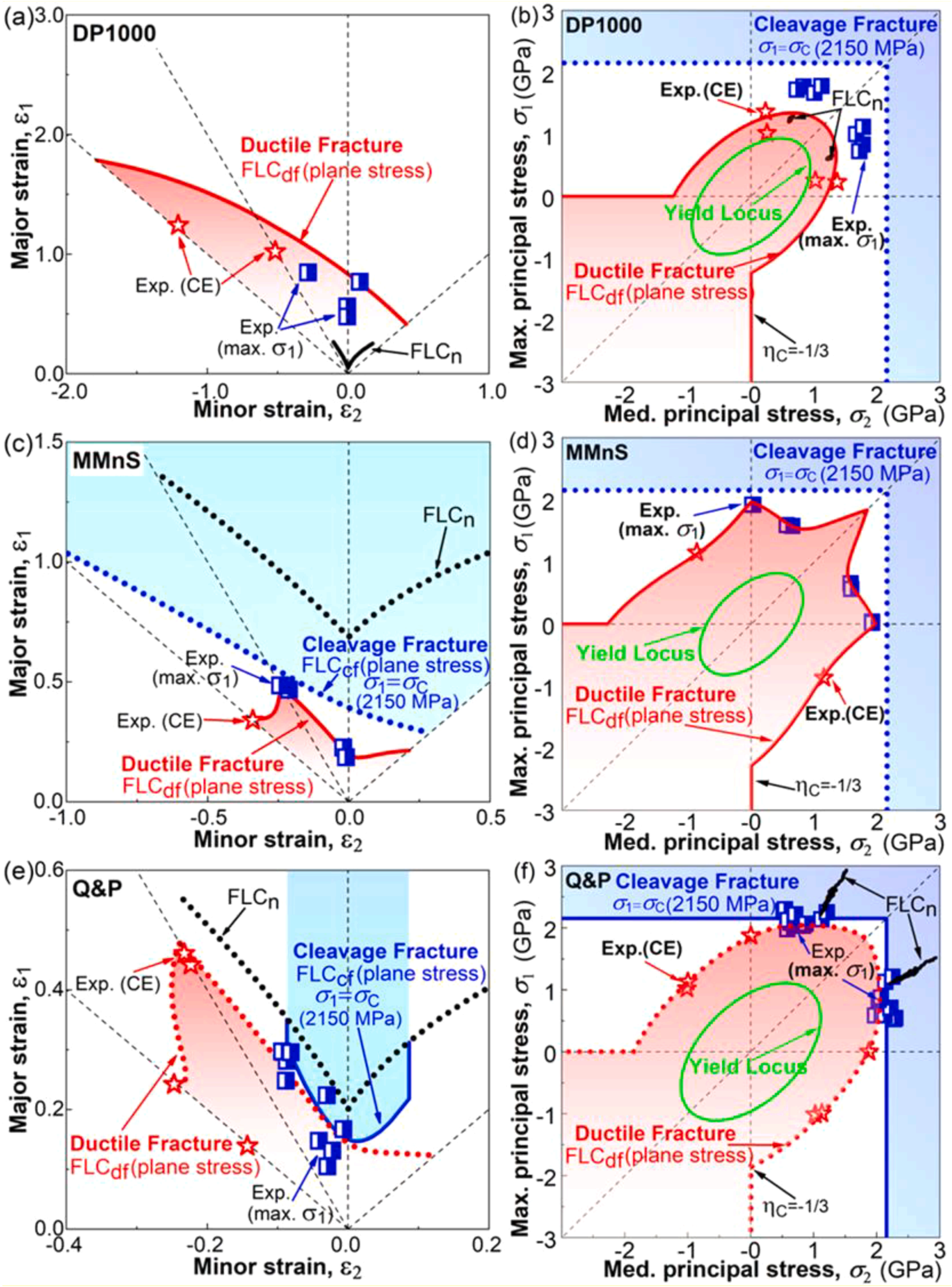

Fig. 11. The forming limit framework considering different failure patterns demonstrated in the space of principal strain (left) and principal stress (right) for three AHSS. (a) and (b) DP1000, (c) and (d) MMnS, (e) and (f) Q&P steel.

7. A forming limit framework accounting for various failure mechanisms

7.1. The concept of the general forming limit framework

A complete forming limit framework should consider the competition and interaction of three failure mechanisms, namely i) localization, ii) ductile, and iii) cleavage fracture, which is demonstrated in Fig. 10 for three different AHSS. **i) Localization** is the most well-known failure pattern in conventional sheet metals, where the forming limit curve at necking (FLC_n) is a widely employed tool to describe the global formability limited by localized deformation. Given the flow curve parameters, the theoretical FLC_n between uniaxial and biaxial tension can be calculated using the MMFC, shown as the black curves in Fig. 10. **ii) Ductile fracture** plays a more important role during the forming processes of AHSS. The ductile fracture loci, represented as stress state-dependent failure strains, are often used to characterize the local formability of AHSS, which are depicted in Fig. 10 for three investigated AHSS. A cutoff value of $\eta_c = -1/3$ in the ductile fracture criterion is assumed for all investigated materials. The ductile fracture loci under loading conditions of plane stress ($\sigma_2 = 0$ or $\sigma_3 = 0$) and generalized plane strain tension ($\overline{\theta} = 0$) are plotted as red curves in the 2D figures, respectively. **iii) Cleavage fracture** is another critical failure mechanism, as revealed in this study, in the forming processes of AHSS, particularly under high triaxiality conditions. Given the flow curve and cleavage fracture strength ($\sigma_c = 2150$ MPa) of the Q&P steel, the cleavage fracture criterion ($\sigma_1 \geq \sigma_c$) is represented as the stress state dependent critical equivalent strain ($\overline{\varepsilon} \geq \overline{\varepsilon}_{\sigma_1=\sigma_c}$), which is shown as the orange surface in Fig. 10(e). Since cleavage fracture is not observed in DP1000 and MMnS and the maximum σ_1 in all specimens is lower than 2150 MPa, the same value can be considered a plausible estimation for the σ_c of these two materials for comparison purposes. The critical strain loci of cleavage fracture under loading conditions of plane stress ($\sigma_2 = 0,$ or $\sigma_3 = 0$) and generalized plane strain tension ($\overline{\theta} = 0$) are plotted as blue curves in the 2D figures, respectively. It should be noted that the cleavage fracture locus is only presented for the failure probability of 50% for visualization purposes. To avoid confusion, a dotted curve will be adopted when the corresponding failure mechanism is not activated in the material.

The forming limit diagram (FLD) and yield locus under plane stress are particularly important in sheet metal forming. The three failure patterns, namely necking, ductile, and cleavage fracture, under plane stress conditions are demonstrated in the FLD and principal stress space in Fig. 11. Since all investigated materials are considered isotropic in this study, the failure patterns in the principal stress space are plotted symmetrically with respect to the diagonal axis of biaxial loading. The theoretically calculated FLC_n using the MMFC represents the stress/strain values in the localized deformation region, which eventually approaches the plane strain tension state. Therefore, the FLC_n is demonstrated as two linear sections (black solid curves) under the plane strain tension (where the stress ratio is 0.5) in the principal stress space. The shape of ductile fracture locus under plane stress conditions, particularly between plane strain and biaxial tension, is significantly affected by its sensitivity of the Lode parameter. The shape of the FLC_{cf} in the FLD is significantly affected by the strain-hardening properties of the material. Near the plane strain tension condition in the FLD, there is a critical region for cleavage fracture, which is narrower for the Q&P steel with the Voce type of hardening behavior than the MMnS that follows the Swift hardening law. To understand the failure process in each material, the instantaneous values of strain and stress variables taken from the critical elements (red stars) and the elements with the maximum σ_1 (blue squares) of each geometry are shown in Fig. 10 and Fig. 11, including all repeating tests. The blue square symbol will be adopted for conditions where the critical positions of σ_1 and $\overline{\varepsilon}$ are identical.

7.2. Failure patterns of different AHSS

Three distinct failure patterns have been observed in the investigated AHSS.

- Ductile fracture occurs after significant necking in DP1000.
- Ductile fracture occurs without the formation of localized necking in MMnS.
- Cleavage fracture occurs without obvious necking in Q&P steel.

It is observed that the cleavage fracture locus is entirely above the ductile fracture locus for DP1000 and MMnS, which is consistent with the failure mechanism analysis that only ductile fracture occurs in both materials. For DP1000, the FLC_n is significantly lower than the FLC_{df} in the range between uniaxial and biaxial tension, leading to ordinary ductile fracture with significantly localized deformation under these stress states. The FLC_{df} of the MMnS is consistently below the FLC_n under the considered stress states ($\eta_c \leq \eta \leq 1$). Consequently, ductile fracture occurs in the investigated MMnS without necking.

The failure mechanism analysis results only validate the cleavage fracture criterion for the Q&P steel. Due to the heterogeneity of microstructure and defects in the Q&P steel, the instantaneous values of strain and stress variables at fracture in all repeating tests are scattered, as shown in Fig. 10 and Fig. 11. However, the local stress and strain variables of critical elements exhibiting the maximum σ_1 fall within the cleavage fracture regime in all specimens of the Q&P steel. The theoretical localization limit FLC_n is above the cleavage fracture criterion, leading to the activation of cleavage fracture without obvious necking in the Q&P steel, though slight thickness reduction is observed in some specimens.

Due to the existence of a threshold value of stress triaxiality η_t below which cleavage fracture cannot be triggered, it is speculated that ductile fracture will ultimately be activated in the investigated Q&P steel under the loading conditions ($\eta_c \leq \eta \leq \eta_t$), though not observed in this study. Particular attention should be paid to the ductile fracture locus of the Q&P steel. The critical-strain-based fracture locus in Fig. 7(a) and Fig. 10(e) is inversely optimized to match the global fracture displacements in different tensile tests of Q&P steel. Reaching the critical-strain-based fracture locus does not necessarily indicate the occurrence of ductile fracture in experiments in the investigated Q&P steel, which is valid only if cleavage fracture was suppressed. Therefore, the calibrated strain-based fracture locus can only be assumed to be the lower boundary of the ductile fracture locus. The stress state in most fracture initiation elements of the Q&P steel is located near the intersection of cleavage and ductile fracture locus, where the ductile fracture strain is almost equal to the cleavage fracture strain. As a result, similar accuracy in predicting fracture displacements of tensile tests can be obtained using the critical-strain-based fracture criterion and cleavage failure criterion. The difference in the predicted fracture initiation position and propagation path in the SH specimen of Q&P steel using two approaches is attributed to the stress state dependent competition between ductile and cleavage fracture.

7.3. Stress-state-dependent competition different failure patterns

To assess the competition between ductile and cleavage fracture, it is of particular interest to analyze the evolution of maximum principal stress under different stress states, as demonstrated in Fig. 12 for three AHSS. When the Mises plasticity model is applied, the corresponding σ_1 at yielding and ductile fracture can be identified using Eq. (3) and Eq. (5) and the corresponding hardening law of the material. It is also evident in Fig. 12 that cleavage fracture is more prone to occur at low temperatures, as the yield strength of metallic materials with bcc structures typically increases with decreasing temperature. It needs to be pointed out that the following discussions on the competition between different fracture mechanisms are based on these hypotheses. i) Crack propagation is the critical step of the cleavage fracture process in the investigated materials; ii) Cleavage fracture is the energetically preferred failure mode compared with ductile fracture; iii) the crack length at cleavage fracture initiation is smaller than that of ductile crack initiated during deformation, the former is in the range of grain size while the latter corresponds to the element size in the current simulation scheme.

Proportional loading conditions: 1) Cleavage fracture is the only failure pattern when the critical values of stress and strain variables (σ_1, $\overline{\varepsilon}$) at cleavage fracture are smaller than those of ductile fracture, e.g., $\eta \geq \eta_t$. 2) Ductile fracture initiation occurs if the critical values of stress and strain variables (σ_1, $\overline{\varepsilon}$) at cleavage fracture are larger than those of ductile fracture. However, in the latter case, the initiated ductile crack (manifested as the first deleted element) might propagate in the cleavage mode if the cleavage fracture strength is reached ($\sigma_1 \geq \sigma_c$) at the crack tip due to local stress concentration. Otherwise, the initiated ductile crack should propagate in the ductile failure mode, e.g., under shear loading conditions. **Non-proportional loading conditions**: Since whether cleavage fracture propagation is triggered or not is only determined by the instantaneous value of σ_1, it is speculated that cleavage fracture is not affected by the non-proportional loading effects. Therefore, only the ductile fracture initiation is affected by the loading history in non-proportional conditions. The competition and transition of failure modes are similar to the proportional loading scenarios.

The simulation results of fracture initiation and propagation in the SH specimens of the Q&P steel are further used to elaborate the stress state dependent competition of failure mechanisms. The evolution of equivalent plastic strain, stress triaxiality and fracture indicators is shown in Fig. 13 for four elements. One element corresponds to crack initiation (red), and the other is located on the crack path (blue) in the simulation results using strain and stress criteria, respectively. Crack initiation occurs under the shear state in the simulation results of strain based criterion. In contrast, the crack initiation site experiences tension loading with the triaxiality of approximately 0.5 when the cleavage fracture criterion is applied. The element (blue) on the shear crack path (strain criterion) experiences the change of stress state from compressive to slight tension, which is deleted due to reaching the ductile fracture criterion ($I_{df} \geq 1$). The element (blue) on the cleavage crack path (stress criterion) experiences a sudden increase of stress triaxiality, from compressive to high triaxial tension, which is deleted due to reaching the cleavage fracture criterion ($\sigma_1 \geq \sigma_c$). When both criteria are activated, the position of crack initiation is determined by the competition in the evolution of fracture indicators (cleavage or ductile), which is governed by the cleavage fracture strength and ductile fracture strains under different stress states. The competition of different failure mechanisms under a broader range of stress states, such as using Nakajima or cross-form specimens under biaxial loading conditions, remains an important topic for further investigation.

7.4. Cleavage fracture sensitivity analysis

Cleavage fracture can be suppressed under low triaxiality loading conditions in the investigated Q&P steel. These observations indicate that the formability of AHSS can be further explored by mitigating the risks of cleavage fracture by controlling the local stress states outside the critical conditions near plane strain tension. In addition, the size and position of the critical region for cleavage fracture in the FLD are governed by material properties, e.g., the cleavage fracture strength and plastic flow properties of different materials. A parametric study on the sensitivity of the cleavage fracture region is performed using the Voce hardening law, assuming the ductile fracture strain is not affected by strain hardening behavior, as shown in Fig. 14. With an increase in σ_c, more plastic deformation is needed to activate cleavage fracture and the cleavage fracture region on the FLD eventually vanishes. The FLC_n (dashed curves) is not affected by the strength parameters, k_0 and Q, which significantly influences the FLC_cf (solid curves). The strain hardening parameter γ significantly impacts both the FLC_n and FLC_cf. Following the Voce-type hardening law, it is observed that a lower yield strength and relatively low hardening component are beneficial for reducing the risk of cleavage fracture.

With the prosperous development of advanced high-strength steels aiming for record-breaking high strength, this research draws attention to the increasing risk of cleavage fracture in metal forming. It also provides an essential insight into the development of high-strength metallic materials, emphasizing that the cleavage fracture strength should be considered as another important parameter in addition to the strength-ductility synergy. From the characteristics of flow curves, a low yield strength followed by a steady strain hardening stage is considered desirable for enhancing global formability and mitigating cleavage fracture. For a quick assessment of

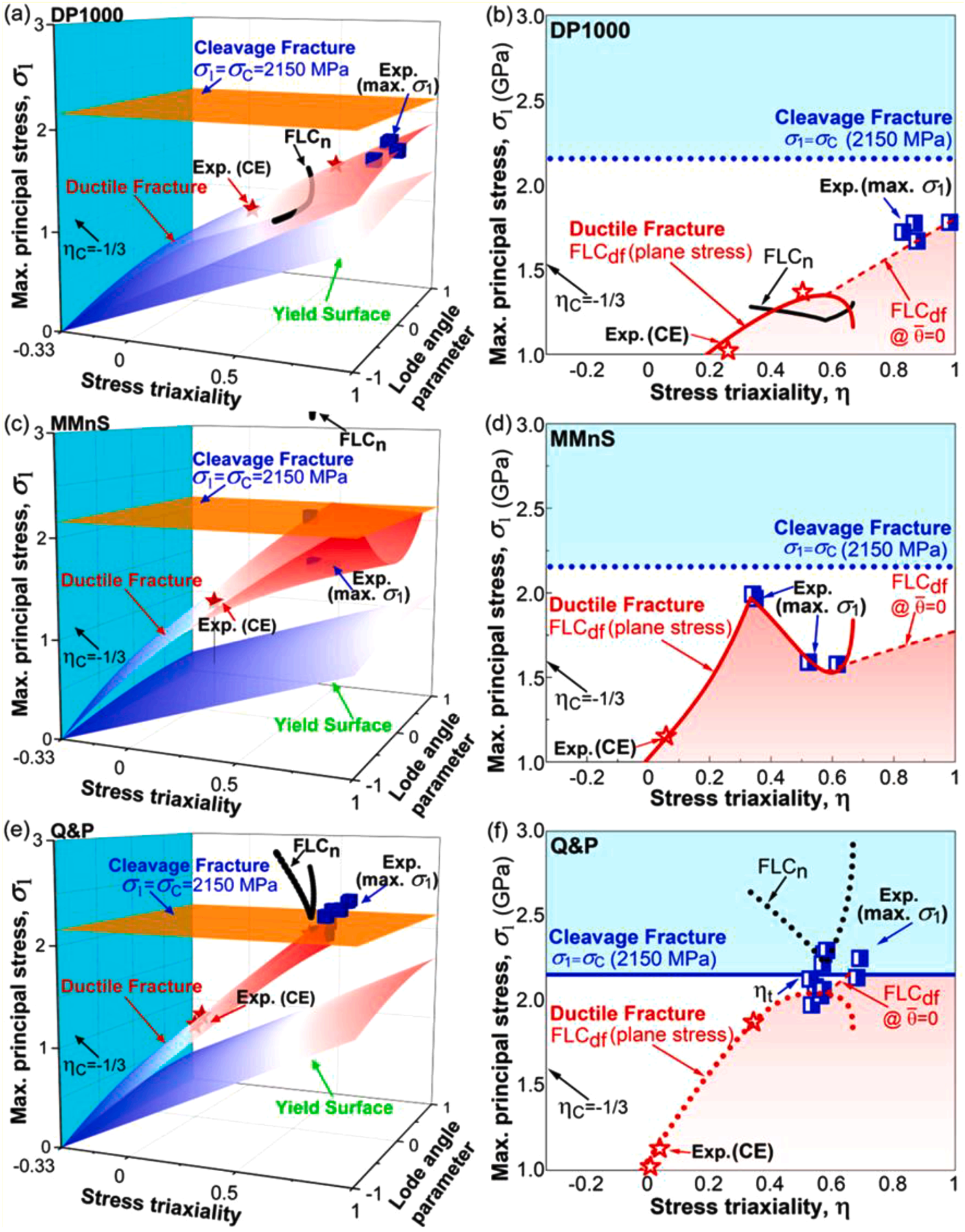

Fig. 12. The forming limit framework considering different failure patterns demonstrated as stress state dependent maximum principal stress for three AHSS. (a) and (b) DP1000, (c) and (d) MMnS, (e) and (f) Q&P steel.

the performance of a high-strength material considering the three failure mechanisms, three mechanical tests could be applied, including uniaxial tension, shear, and plane-strain tension or bending tests. The uniaxial tension and shear tests can be used to identify the flow curve of the material. The failure strain in shear and bending tests can be used to rapidly determine the lower boundary of the ductile fracture locus. The cleavage strength can be determined if a cleavage fracture occurs in any of these three tests. If ductile fracture occurs in all these tests, one can make a fast and conservative evaluation of the threshold triaxiality of cleavage fracture (η_t) by using the flow curve and an assumed value of the cleavage fracture strength.

8. Summary

The study focused on investigating and comparing the forming limits and fracture properties of three different types of advanced

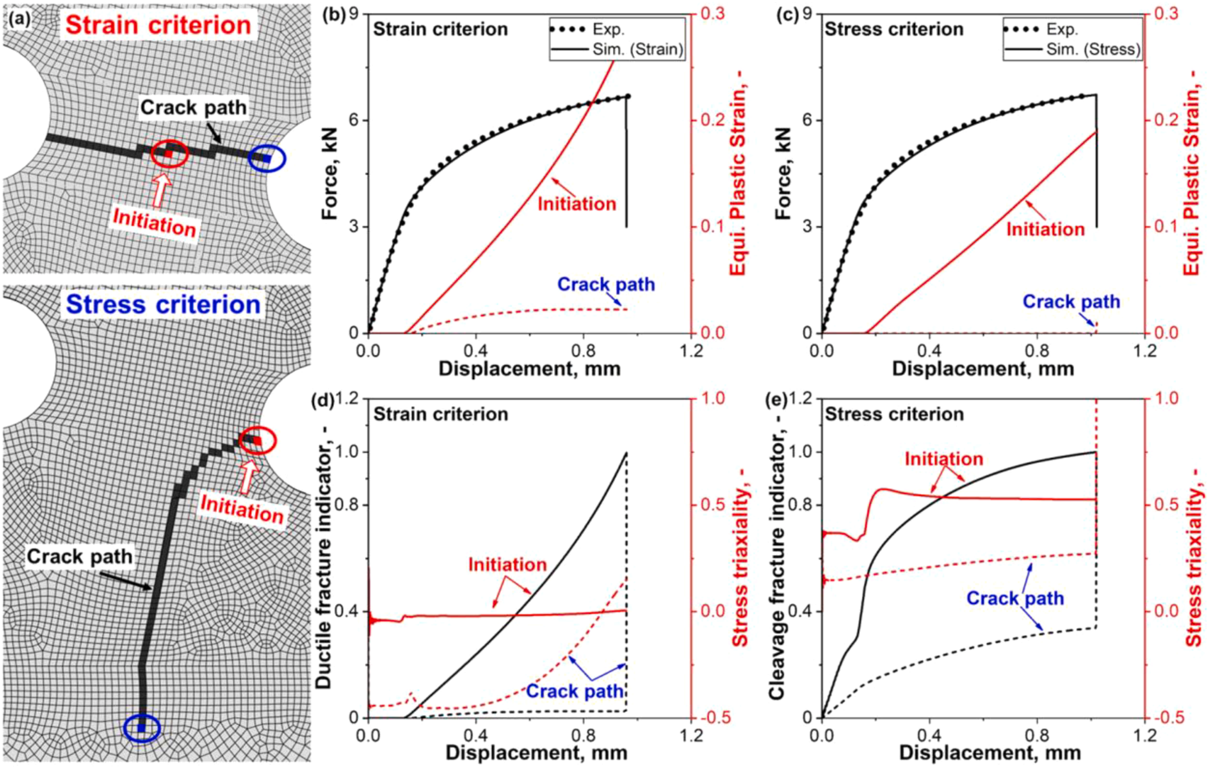

Fig. 13. The evolution of strain, triaxiality and fracture indicators taken from different elements on the crack path in the shear specimen of Q&P steel simulated using strain and stress criteria. (a) crack patterns, (b) and (c) strain history, (d) and (e) triaxiality and fracture indicator.

high-strength steels (AHSS). The global formability, specifically necking resistance, was evaluated using the modified maximum force criterion to calculate the theoretical forming limits at necking. For assessing the local formability, stress state dependent fracture strains were determined using damage mechanics approaches based on tensile tests of various specimens. The key conclusions from the study are as follows:

- Cleavage fracture can be a significant failure pattern that governs the forming limits of advanced high-strength steels. This phenomenon was observed at room temperature under metal forming relevant stress states in a laboratory AHSS sample with superior tensile properties.
- The investigated advanced high-strength steels exhibited various failure patterns, including ductile or cleavage fracture with or without necking. The competition between these failure mechanisms was found to be influenced by material properties and loading conditions.
- The forming limit framework is further extended to incorporate the cleavage failure mechanism, which shows high efficiency in characterizing the competition between different failure mechanisms in the space of critical strain and principal stress.
- Cleavage fracture forming limit shows also high stress state dependency and this dependency changes considerably depending on the material hardening behavior. With the proposed forming limit framework, forming strategies can be designed to avoid the cleavage fracture regime.
- The cleavage fracture strength should be considered an essential parameter in the development of advanced metallic materials besides the strength-ductility synergy obtained from uniaxial tensile tests. A simple testing program is proposed to rapidly screen mechanical performance, considering different failure mechanisms.

CRediT authorship contribution statement

Fuhui Shen: Writing – original draft, Visualization, Software, Methodology, Investigation, Formal analysis, Data curation, Conceptualization. **Yannik Sparrer:** Software, Investigation, Data curation. **Jing Rao:** Data curation, Investigation, Software, Writing – review & editing. **Markus Könemann:** Writing – review & editing. **Sebastian Münstermann:** Writing – review & editing, Resources, Funding acquisition. **Junhe Lian:** Writing – review & editing, Visualization, Validation, Supervision, Methodology, Conceptualization.

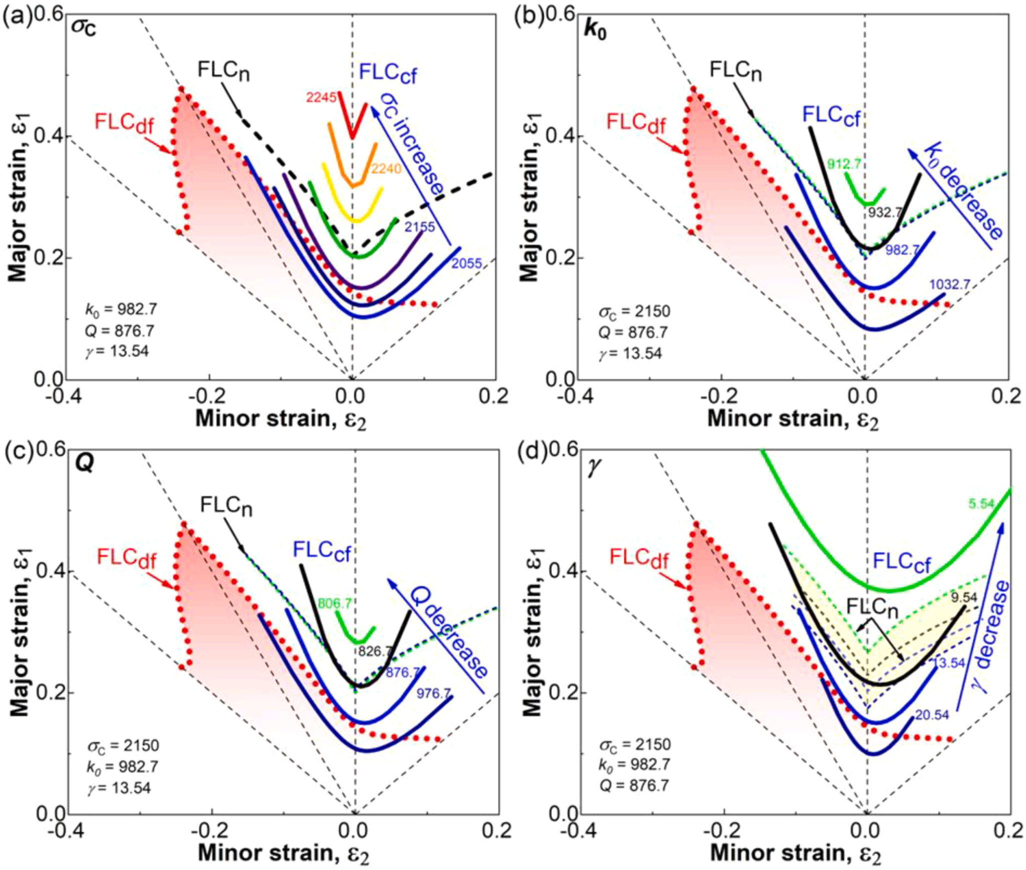

Fig. 14. The sensitivity of cleavage fracture region with respect to (a) cleavage fracture strength σ_c and strain hardening parameter, (b) k_0, (c) Q, and (d) γ in the Voce hardening law $\sigma_{Voce} = k_0 + Q \cdot (1 - exp(- \gamma \cdot \bar{\varepsilon}^p))$. FLC$_{cf}$ is represented by solid curves, and FLC$_n$ is represented by dashed curves.

Declaration of competing interest

The authors declare that they have no known competing financial interests or personal relationships that could have appeared to influence the work reported in this paper.

Data availability

Data will be made available on request.

Acknowledgments

Simulations were performed with computing resources granted by RWTH Aachen University under projects rwth0241 and rwth0779.

Appendix A. Anisotropic plasticity of DP1000

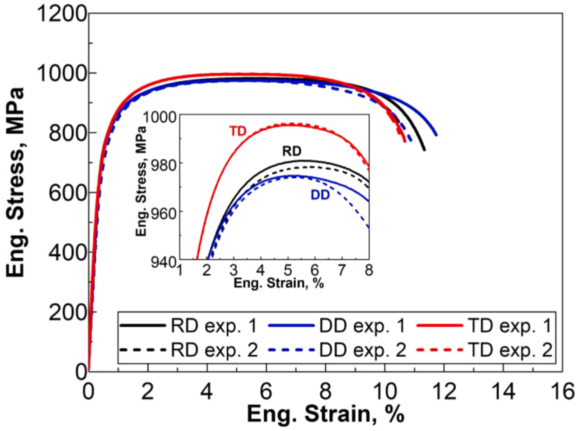

Fig. A1. Engineering stress-strain curves of DP1000 from uniaxial tensile tests along different directions.

Table A1
Uniaxial tensile properties of DP1000 tested along different directions.

Material	RD		DD		TD	
	Test 1	Test 2	Test 1	Test 2	Test 1	Test 2
Yield strength (YS), MPa	780.9	777.8	752.3	748.8	752.5	741.2
Ultimate tensile strength (UTS), MPa	981.0	978.4	974.7	974.0	995.7	996.3
Uniform elongation (UE),%	4.9	5.3	4.9	4.9	4.8	4.9
Total elongation (TE),%	11.0	10.2	11.4	10.5	10.3	10.1

References

Bai, Y., Wierzbicki, T., 2008. A new model of metal plasticity and fracture with pressure and Lode dependence. Int. J. Plast. 24, 1071–1096.

Bai, Y., Wierzbicki, T., 2010. Application of extended Mohr–Coulomb criterion to ductile fracture. Int J Fracture 161, 1–20.

Bao, Y., Wierzbicki, T., 2005. On the cut-off value of negative triaxiality for fracture. Eng. Fract. Mech 72, 1049–1069.

Beremin, F.M., 1983. A local criterion for cleavage fracture of a nuclear pressure vessel steel. Metallurg. Transac. A 14, 2277–2287.

Brünig, M., Gerke, S., Schmidt, M., 2018. Damage and failure at negative stress triaxialities: experiments, modeling and numerical simulations. Int. J. Plast. 102, 70–82.

Chung, K., Kim, H., Lee, C., 2014. Forming limit criterion for ductile anisotropic sheets as a material property and its deformation path insensitivity. Part I: deformation path insensitive formula based on theoretical models. Int. J. Plast. 58, 3–34.

Gao, P.F., Fei, M.Y., Zhan, M., Fu, M.W., 2023. Microstructure- and damage-nucleation-based crystal plasticity finite element modeling for the nucleation of multi-type voids during plastic deformation of Al alloys. Int. J. Plast. 165.

Habib, S.A., Lloyd, J.T., Meredith, C.S., Khan, A.S., Schoenfeld, S.E., 2019. Fracture of an anisotropic rare-earth-containing magnesium alloy (ZEK100) at different stress states and strain rates: experiments and modeling. Int. J. Plast. 122, 285–318.

Heibel, S., Dettinger, T., Nester, W., Clausmeyer, T., Tekkaya, A.E., 2018. Damage mechanisms and mechanical properties of high-strength multiphase steels. Materials (Basel) 11, 761.

Hora, P., Tong, L., Berisha, B., 2011. Modified maximum force criterion, a model for the theoretical prediction of forming limit curves. Int. J. Material Forming 6, 267–279.

Isik, K., Silva, M.B., Tekkaya, A.E., Martins, P.A.F., 2014. Formability limits by fracture in sheet metal forming. J. Mater. Process. Technol. 214, 1557–1565.

Jacobs, T.R., Matlock, D.K., Findley, K.O., 2019. Characterization of localized plastic deformation behaviors associated with dynamic strain aging in pipeline steels using digital image correlation. Int. J. Plast.

Johnson, G.R., Cook, W.H., 1985. Fracture characteristics of three metals subjected to various strains, strain rates, temperatures and pressures. Eng. Fract. Mech 21, 31–48.

Khan, A.S., Liu, H.W., 2012. A new approach for ductile fracture prediction on Al 2024-T351 alloy. Int. J. Plast. 35, 1–12.

Li, F.F., Fang, G., 2022. Stress-state dependency of ductile fracture in an extruded magnesium alloy and its underlying mechanisms. Int. J. Plast. 152.

Li, H., Fu, M.W., Lu, J., Yang, H., 2011. Ductile fracture: experiments and computations. Int. J. Plast. 27, 147–180.

Li, S., He, J., Gu, B., Zeng, D., Xia, Z.C., Zhao, Y., Lin, Z., 2018. Anisotropic fracture of advanced high strength steel sheets: experiment and theory. Int. J. Plast. 103, 95–118.

Li, X., Roth, C.C., Bonatti, C., Mohr, D., 2022. Counterexample-trained neural network model of rate and temperature dependent hardening with dynamic strain aging. Int. J. Plast. 151.

Lian, J., Sharaf, M., Archie, F., Münstermann, S., 2013. A hybrid approach for modelling of plasticity and failure behaviour of advanced high-strength steel sheets. Int. J. Damage Mech. 22, 188–218.

Liu, W., Hao, Y., 2021. Damage and fracture prediction of 7075 high-strength aluminum alloy during cryogenic stamping process. Mech. Mater. 163.

Liu, W., Lian, J., Aravas, N., Münstermann, S., 2020a. A strategy for synthetic microstructure generation and crystal plasticity parameter calibration of fine-grain-structured dual-phase steel. Int. J. Plast. 126, 102614.

Liu, W., Lian, J., Münstermann, S., Zeng, C., Fang, X., 2020b. Prediction of crack formation in the progressive folding of square tubes during dynamic axial crushing. Int. J. Mech. Sci. 176, 105534.

Lou, Y., Chen, L., Clausmeyer, T., Tekkaya, A.E., Yoon, J.W., 2017. Modeling of ductile fracture from shear to balanced biaxial tension for sheet metals. Int. J. Solids Struct 112, 169–184.

Lou, Y., Huh, H., Lim, S., Pack, K., 2012. New ductile fracture criterion for prediction of fracture forming limit diagrams of sheet metals. Int J Solids Struct 49, 3605–3615.

Lou, Y., Yoon, J.W., Huh, H., 2014. Modeling of shear ductile fracture considering a changeable cut-off value for stress triaxiality. Int. J. Plast. 54, 56–80.

Marciniak, Z., Kuczyński, K., 1967. Limit strains in the processes of stretch-forming sheet metal. Int. J. Mech. Sci. 9, 609–620.

Mohr, D., Marcadet, S.J., 2015. Micromechanically-motivated phenomenological Hosford–Coulomb model for predicting ductile fracture initiation at low stress triaxialities. Int. J. Solids Struct 67-68, 40–55.

Mu, L., Jia, Z., Ma, Z., Shen, F., Sun, Y., Zang, Y., 2020. A theoretical prediction framework for the construction of a fracture forming limit curve accounting for fracture pattern transition. Int. J. Plast. 129, 102706.

Mu, L., Zang, Y., Wang, Y., Li, X.L., Araujo Stemler, P.M., 2018. Phenomenological uncoupled ductile fracture model considering different void deformation modes for sheet metal forming. Int. J. Mech. Sci. 141, 408–423.

Orowan, E., 1949. Fracture and strength of solids. Repor. Progress Phys 12, 185–232.

Park, N., Huh, H., Lim, S.J., Lou, Y., Kang, Y.S., Seo, M.H., 2017. Fracture-based forming limit criteria for anisotropic materials in sheet metal forming. Int. J. Plast. 96, 1–35.

Park, N., Huh, H., Yoon, J.W., 2018. Anisotropic fracture forming limit diagram considering non-directionality of the equi-biaxial fracture strain. Int. J. Solids Struct 151, 181–194.

Peirs, J., Verleysen, P., Degrieck, J., 2011. Novel technique for static and dynamic shear testing of Ti6Al4V sheet. Exp. Mech 52, 729–741.

Peng, L.F., Xu, Z.T., Fu, M.W., Lai, X.M., 2017. Forming limit of sheet metals in meso-scale plastic forming by using different failure criteria. Int. J. Mech. Sci. 120, 190–203.

Peng, Z., Zhao, H., Li, X., 2021. New ductile fracture model for fracture prediction ranging from negative to high stress triaxiality. Int. J. Plast. 145.

Pineau, A., Benzerga, A.A., Pardoen, T., 2016. Failure of metals I: brittle and ductile fracture. Acta Mater 107, 424–483.

Quach, H., Kim, J.J., Nguyen, D.T., Kim, Y.S., 2020. Uncoupled ductile fracture criterion considering secondary void band behaviors for failure prediction in sheet metal forming. Int. J. Mech. Sci. 169.

Rahmaan, T., Abedini, A., Butcher, C., Pathak, N., Worswick, M.J., 2017. Investigation into the shear stress, localization and fracture behaviour of DP600 and AA5182-O sheet metal alloys under elevated strain rates. Int. J. Impact Eng 108, 303–321.

Roth, C.C., Mohr, D., 2016. Ductile fracture experiments with locally proportional loading histories. Int. J. Plast. 79, 328–354.

Roth, C.C., Mohr, D., 2018. Determining the strain to fracture for simple shear for a wide range of sheet metals. Int. J. Mech. Sci. 149, 224–240.

Shen, F., Münstermann, S., Lian, J., 2020. An evolving plasticity model considering anisotropy, thermal softening and dynamic strain aging. Int. J. Plast. 132, 102747.

Shen, F., Münstermann, S., Lian, J., 2022a. A unified fracture criterion considering stress state dependent transition of failure mechanisms in bcc steels at –196°C. Int. J. Plast. 156.

Shen, F., Münstermann, S., Lian, J., 2023. Cryogenic ductile and cleavage fracture of bcc metallic structures – influence of anisotropy and stress states. J. Mech. Phys. Solids 176.

Shen, F., Wang, H., Liu, Z., Liu, W., Könemann, M., Yuan, G., Wang, G., Münstermann, S., Lian, J., 2022b. Local formability of medium-Mn steel. J. Mater. Process Tech 299.

Tekkaya, A.E., Bouchard, P.O., Bruschi, S., Tasan, C.C., 2020. Damage in metal forming. CIRP Annals 69, 600–623.

Torki, M.E., Keralavarma, S.M., Benzerga, A.A., 2021. An analysis of Lode effects in ductile failure. J. Mech. Phys. Solids 153, 104468.

Wang, P., Qu, S., 2018. Analysis of ductile fracture by extended unified strength theory. Int. J. Plast. 104, 196–213.

Wang, X., Fan, X., Chen, X., Yuan, S., 2022. Cryogenic deformation behavior of 6061 aluminum alloy tube under biaxial tension condition. J. Mater. Process. Technol. 303.

Wang, H., Shen, F.i, Wang, Y., Yan, F., Chang, Z., Yu, C., Kang, J., Sebastian, M., 2023. Effect of tempering temperature on the microstructure, deformation and fracture properties of an ultrahigh strength medium-Mn steel processed by quenching and tempering. Steel Res. Int. 94, 2200902 https://doi.org/10.1002/srin.202200902.

Wu, B., Li, X., Di, Y., Brinnel, V., Lian, J., Münstermann, S., 2017. Extension of the modified Bai-Wierzbicki model for predicting ductile fracture under complex loading conditions. Fatigue Fract. Engineer. Mater. Struc. 40, 2152–2168.

Xiong, Z., Jacques, P.J., Perlade, A., Pardoen, T., 2018. Ductile and intergranular brittle fracture in a two-step quenching and partitioning steel. Scr. Mater 157, 6–9.

Yang, F., Luo, H., Pu, E., Zhang, S., Dong, H., 2018. On the characteristics of Portevin–Le Chatelier bands in cold-rolled 7Mn steel showing transformation-induced plasticity. Int. J. Plast. 103, 188–202.

Yang, H., Li, H., Sun, H., Zhang, Y.H., Liu, X., Zhan, M., Liu, Y.L., Fu, M.W., 2022. Anisotropic plasticity and fracture of alpha titanium sheets from cryogenic to warm temperatures. Int. J. Plast. 156.

Yuan, S., Cheng, W., Liu, W., 2021. Cryogenic formability of a solution-treated aluminum alloy sheet at low temperatures. J. Mater. Processing Technol. 298.

Zheng, L., Wang, Z., Meng, B., Wan, M., 2023. A unified ductile fracture criterion suitable for sheet and bulk metals considering multiple void deformation modes. Int. J. Plast. 164.